Supplement

to

A Near-Field Gaussian Plume Inversion Flux Quantification Method, Suitable For Unmanned Aerial Vehicle Sampling

by Adil Shah *et al.*

Contents

H. Random walk simulation results

Figure S7. $F_{e,\,v,\,i}$ values, simulating flight 3 from the sample data, as a function of t (blue crosses), plotted against left-hand axis, with F_t (black line) also shown.

Table S5. Flux convergence parameters required to approximate the fundamental threshold uncertainty associated with flux measurements as a function of sampling time, which are unique for each flight in the sample data.

Table S6. Average virtual test F_e values for each flight in the sample data with eight hours of random sampling of a static plume.

I. Initial flux results, uncertainty factors and uncertainty analysis

Table S7. Initial flux values and corresponding fractional lower and upper uncertainty bounds, for each flight from the sample data.

Table S8. A comparison between ΔF_{-}^{me} and ΔF_{-}^{mo} for each flight from the sample data, as a fraction of ΔF_{-}.

Table S9. A comparison between $\Delta F_{-}^{me,\,U(z)}$, $\Delta F_{-}^{me,\,\rho}$ and $\Delta F_{-}^{me,\,ib}$ for each flight from the sample data, as a fraction of ΔF_{-}^{me}.

References

A. Notation

UAV: unmanned aerial vehicle
NGI: near field Gaussian plume inversion
$[CH_4]$: atmospheric methane concentration
TDM: tracer dispersion method
NPL: UK National Physical Laboratory
q_{me}: measured flux density
θ: mean wind direction
UGGA: Los Gatos Research, Inc. Ultra-portable Greenhouse Gas Analyzer
CRF: NPL Controlled Release Facility
z: height above ground level
x: distance from the source along the mean wind vector
y: horizontal distance perpendicular to mean wind direction
$[CH_4]_{me}$: $[CH_4]$ as a function of x, y and z
$[CH_4]_0$: background methane concentration
σ_b: background uncertainty
$U(z)$: continuous wind speed
$\sigma_U(z)$: wind speed variability
ρ: atmospheric methane mass density
σ_ρ: uncertainty in ρ
Δq_{me}: uncertainty in q_{me}
$\sigma_i([CH_4])$: instrumental uncertainty factor
F_e: initial flux estimate
q_{mo}: modelled flux density
$\sigma_y(x)$: crosswind mixing factor
$\sigma_z(x)$: vertical mixing factor
y_c: centre of the plume in the y direction
h: emission height
τ_y: crosswind mixing factor evaluated at a distance of 1 m
τ_z: vertical mixing factor evaluated at a distance of 1 m
$q_{me,\,y}$: q_{me} with the z Gaussian component removed
$\tau_{z,\,max}$: maximum constraining value of τ_z
ΔF_m: measurement uncertainty in F_e
ΔF_-: total minimum uncertainty
ΔF_+: total maximum uncertainty
F_t: prescribed modelled point source target flux
L: length
$\delta\theta$: change in angle (in magnitude but not in sign) between each successive step in the random walk
θ_R: initial random direction
t: simulated sampling time
$F_{e,\,v}$: virtual flux estimate

$\overline{F_{e,v}}$: average value of $F_{e,v}$
A: flux anomaly
α: anomaly coefficient
β: anomaly decay constant
A_f: inherent limiting uncertainty
$t_{1\%}$: % fundamental uncertainty sampling threshold
CFD: computation fluid dynamics

B. CRF flux release

The NPL CRF is computer controlled, containing thermal mass flow controllers, which allow a steady high-precision release rate of a gas from up to four configurable release nodes, described in detail by Gardiner et al. (2017). The natural gas methane source used for each of the four flux releases was certified for purity by the NPL (certification reference number 2016120240-3) by comparison with metrological traceable gas standards. Releases times are given in Table S1. All times in Table S1 are quoted in seconds past midnight (spm) local time on the day of measurement. The CRF flux uncertainties given in Table S1 are expanded uncertainties; that is to say they are standard uncertainties multiplied by a coverage factor (k = 2) to provide a coverage probability of approximately 95%.

CRF release number	Date	Period of emission (spm)	Longitude/ °E	Latitude/°N	CRF flux/g s^{-1}	TDM (Team A) flux/g s^{-1}	TDM (Team B) flux/g s^{-1}
1	2.11.2016	54000 – 59700	-00.42331	+52.10498	3.0±0.2	2.9±0.7	2.8±0.5
2	3.11.2016	37860 – 44340	-00.42474	+52.10356	3.0±0.2	3.3±0.8	2.9±0.5
3	3.11.2016	51960 – 55740	-00.42419	+52.10343	3.0±0.2	2.9±0.7	3.1±0.6
4	3.11.2016	56160 – 60000	-00.42419	+52.10343	1.5±0.1	1.7±0.4	1.2±0.2

Table S1. Reported CRF methane flux releases with the time duration of continuous methane emission given in seconds past midnight (spm), local time (GMT). The GPS position of the flux release was reported by the NPL from the position of the release nodes. Calculated fluxes using the tracer dispersion method (TDM) are also given here.

Alongside the UAV NGI fluxes, fluxes were independently derived by two separate teams (Team A and Team B), to verify the CRF emission fluxes and to provide an alternative to UAV sampling. These tracer fluxes are also given in Table S1, along with the total standard error in the flux. The tracer dispersion method flux quantification methodology has been described elsewhere (Fredenslund et al., 2019).

C. UAV flights

The University of Manchester adapted DJI S900 hexacopter UAV (see Figure S1) had a total take-off mass of ~5.5 kg (including battery). The individual flight tracks and CRF release points (Table S2) are shown in Figure S2.

Figure S1. A photograph of the UAV platform at rest (without battery), with the PFA tubing pointing upwards.

Flight number (colour)	Date	Time of flight (spm)	Flux release number
1 (yellow)	2.11.2016	55781 – 57037	1
2 (red)	2.11.2016	57805 – 58920	1
3 (blue)	3.11.2016	40640 – 42320	2
4 (orange)	3.11.2016	*42990 – 43495; 43975 – 44260	2
5 (grey)	3.11.2016	52420 – 53678	3
6 (cyan)	3.11.2016	54178 – 55540	3
7 (green)	3.11.2016	56730 – 58055	4
8 (magenta)	3.11.2016	58780 – 60042	4

Table S2. UAV flight details and flight track colours. The period of each flight is expressed in seconds past midnight (spm), local time (GMT). * Flight 4 was composed of two parts within a single flight as the tether kinked during the omitted sampling period.

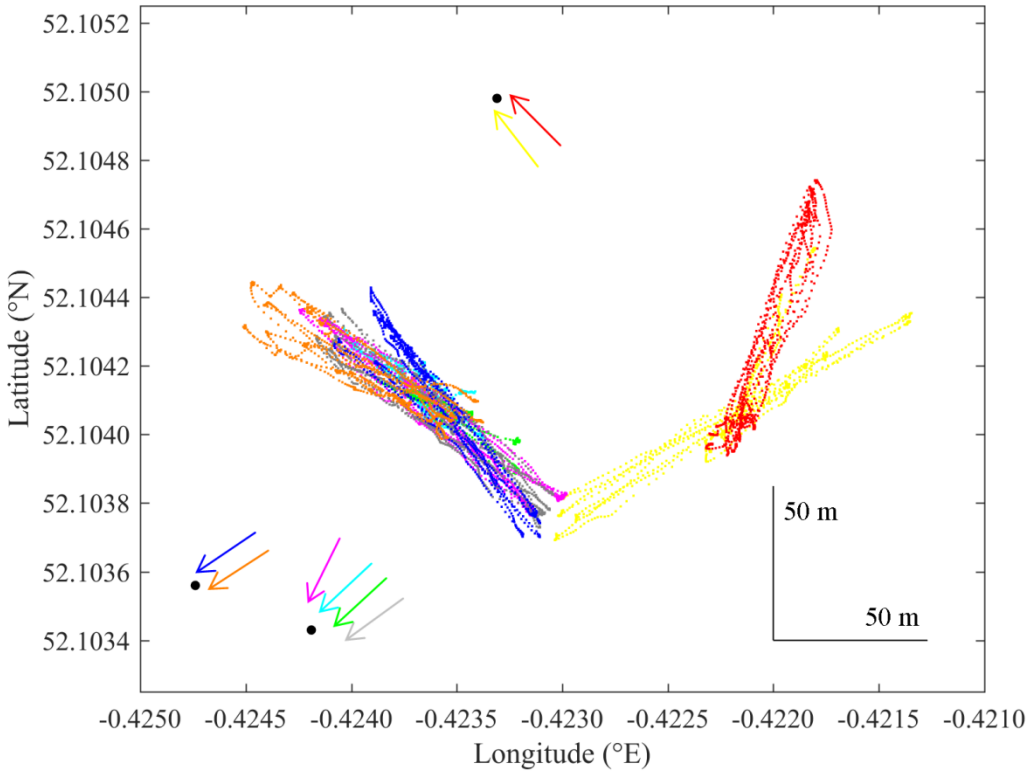

Figure S2. Aerial view of the three emission source locations (black dots) and flight tracks (coloured dots). The coloured dots corresponding to each flight are given in Table S2. The wind direction for each flight is represented by an arrow in the same colour as the flight track. The position of the emission source for each flight is the dot nearest to its corresponding arrow.

D. Assigning a background concentration for each flux

Equation (3) relies on a unique value of $[CH_4]_0$ for each sampling experiment, to account for natural background changes that may occur over time. $[CH_4]_0$ was derived for the sample data by plotting $[CH_4]_{me}$ measurements as a histogram (see Figure S3 (a) for example), with an average of 0.1 unique concentration measurements in each histogram bin. In the absence of any plume measurements we would expect measurements of background air to be normally distributed (due to measurement error and natural variability) but the presence of the plume acts to skew this distribution towards higher concentrations. This results in a log-normal distribution for background data and small enhancements in concentration (blue line in Figure S3 (b)). The peak of the fit was taken as $[CH_4]_0$ and the square root of the variance was taken as σ_b. $[CH_4]_0$ values for each flight for the sample data are given in Table S3. The number of $[CH_4]_{me}$ measurements in each histogram bin could be adjusted until a log-normal distribution was visible.

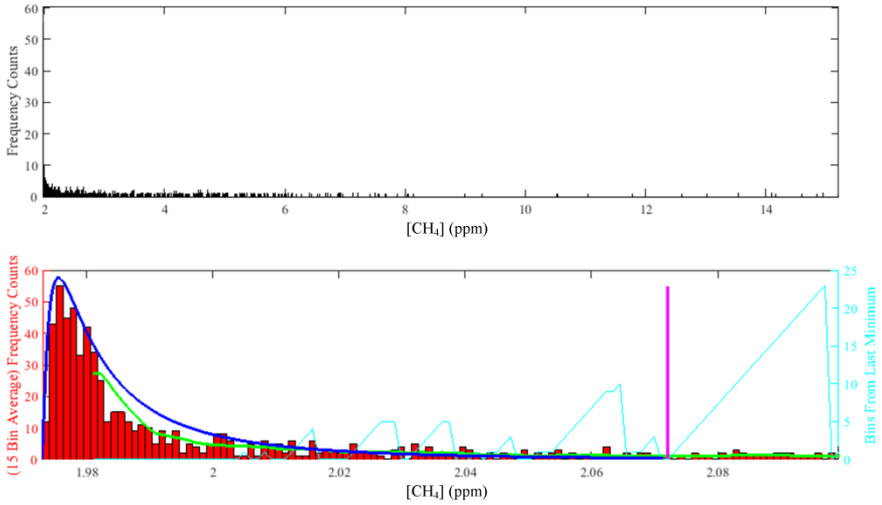

Figure S3. (a) A histogram of methane concentration measurements obtained throughout flight 1 from the sample data. (b) A histogram of the lowest concentration measurements from flight 1 (red bars) with 15-bin-averages (green line) and log-normal function fit (blue line) plotted against the left hand axis. The number of bins prior to the previous 15-bin average minimum has been plotted in cyan against the right hand axis. The first minimum with 15 subsequent averages less than the minimum has been indicated by the magenta line.

UAV flight	**($[CH_4]_0 \pm \sigma_b$)/ppm**
1	1.98±0.03
2	1.98±0.05
3	1.98±0.01
4	1.99±0.04
5	1.97±0.01
6	1.97±0.01
7	1.96±0.01
8	1.97±0.01

Table S3. Calculated background concentrations for each flight from the sample data.

In order to define a background peak from the full histogram, a 15-bin-average was derived for each bin for each histogram in the sample data (green line in Figure S3(b) for example). This allowed us to define a threshold above which the 15-bin-average started to increase, representing plume interference into the background, serving as the limit to which a log-normal distribution (blue line in Figure S3(b) for example) could be applied to background concentration measurements. For each bin in the histogram, the minimum 15-bin-average was recorded up to that point from the minimum concentration upwards (the cyan line in Figure S3(b) for example). If at any point, 15 consecutive 15-bin-averages failed to surpass this minimum, the position of that particular minimum on the histogram was defined as the limit (the magenta line in Figure S3(b) for example) to which a log-normal fit could be applied.

A background concentration for the sample data was acquired using the lowest concentration measurements, as it was assumed that the UAV was able to capture background concentration measurements, due to a sufficient extent of spatial sampling. If the background concentration distribution did not express a log-normal trend, it may be more suitable to employ other means of background derivation. This may include separate sampling upwind of the plume.

E. Testing assumption of linearity in $\sigma_y(x)$ and $\sigma_z(x)$

The NGI method assumes $\sigma_y(x)$ and $\sigma_z(x)$ to increase linearly as a function of x. In order to test this assumption, $\sigma_y(x)$ and $\sigma_z(x)$ were derived using the equations found in pages 2- 8, 2- 9 and 2- 11 of Turner (1994). These equations model $\sigma_y(x)$ and $\sigma_z(x)$ as a function of x for different stability classes. $\sigma_y(x)$ and $\sigma_z(x)$ for each stability class is plotted in Figure S4 and Figure S5, respectively. To demonstrate the closeness of these fits to linearity, $\sigma_y(x)$ and $\sigma_z(x)$ was calculated at 100 m for each stability class and then plotted as a linear function of x in for $\sigma_y(x)$ and $\sigma_z(x)$ in Figure S4 and Figure S5, respectively. These plots show that from a near-field sampling plane of less than 500 m from the source, $\sigma_y(x)$ and $\sigma_z(x)$ are almost linear, within approximately 40 m of x.

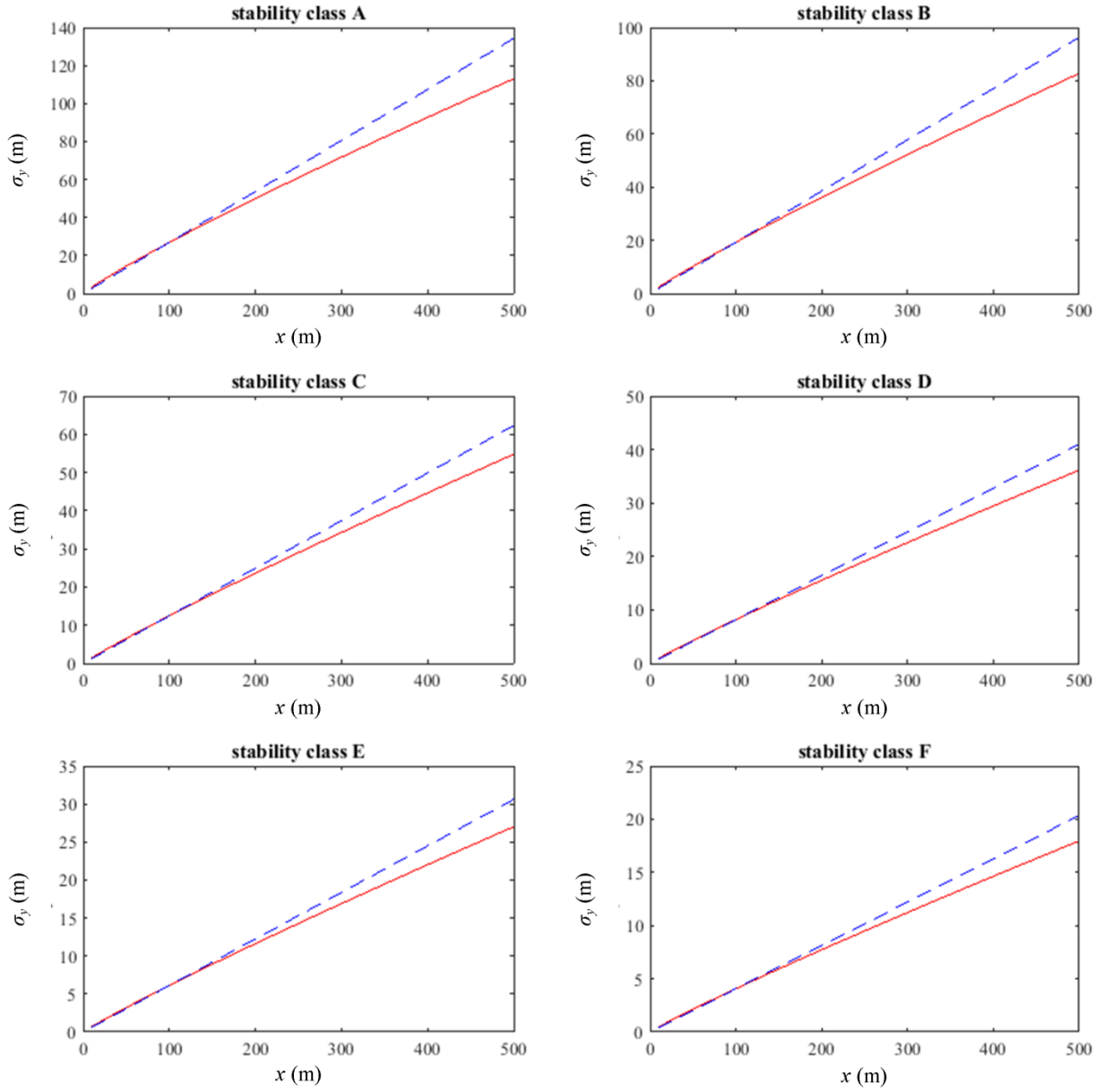

Figure S4. $\sigma_y(x)$ plotted for various stability classes (red lines) using the equations in Turner (1994). The blue dashed line assumes $\sigma_y(x)$ to increase linearly with x, using $\sigma_y(x)$ calculated at 100 m from the equations in Turner (1994).

205

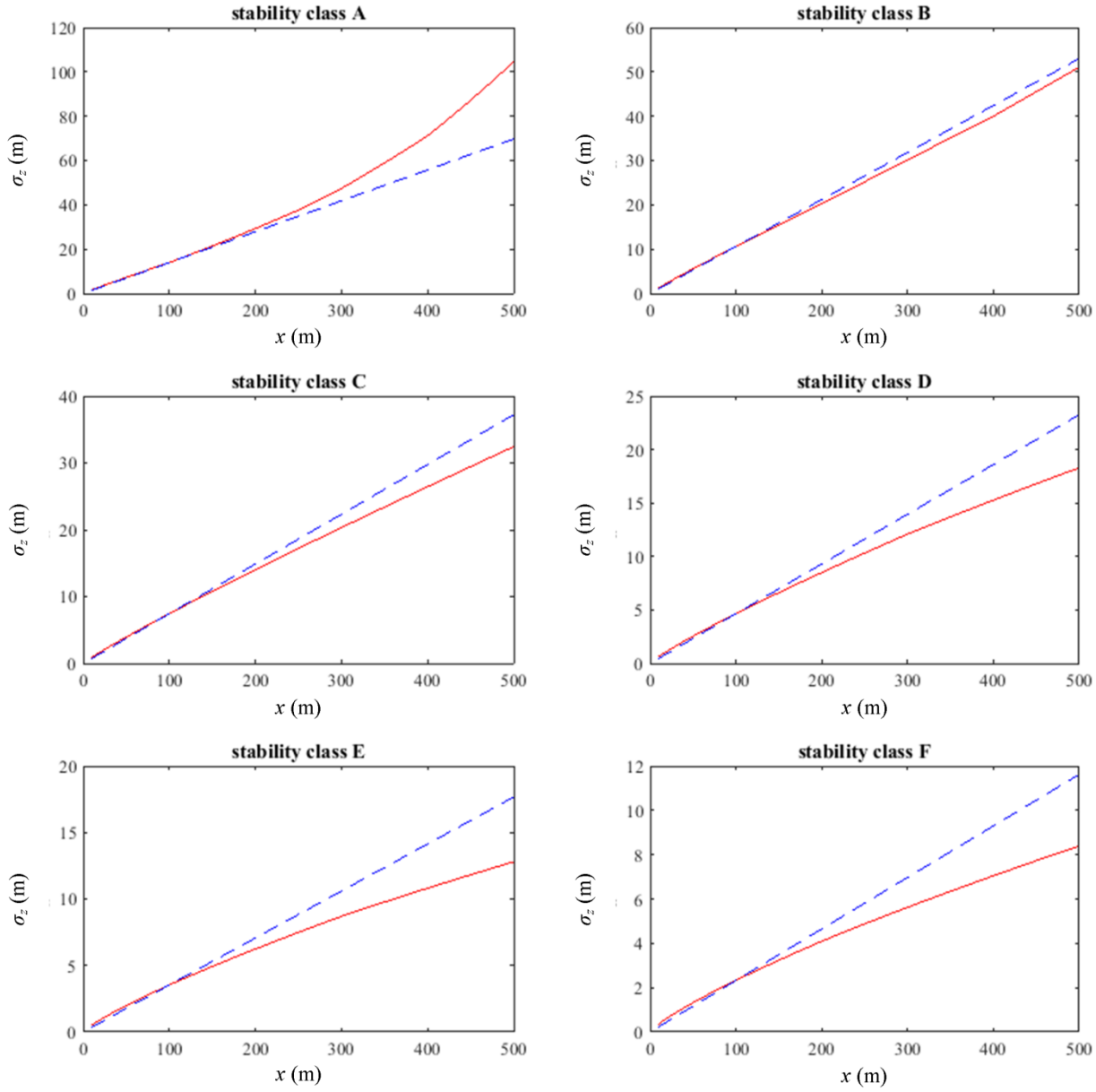

Figure S5. $\sigma_z(x)$ plotted for various stability classes (red lines) using the equations in Turner (1994). The blue dashed line assumes $\sigma_z(x)$ to increase linearly with x, using $\sigma_z(x)$ calculated at 100 m from the equations in Turner (1994).

210

F. Gaussian plume parameters

Values of y_c, τ_y and τ_z derived using the NGI flux quantification method for each UAV flight from the sample data are given in Table S4. These values were used to generate virtual q_{me} values in the random walk simulation. An initial value of $\sigma_z(x)$ was approximated using a Pasquill stability class, at the mean value of x weighted by q_{me} (x_c), which was calculated using each "j" value of q_{me} and x using equation (A).

(A) $$x_c = \frac{\Sigma_j\left(q_{me_j} \cdot x_j\right)}{\Sigma_j\left(q_{me_j}\right)}$$

UAV flight	y_c**/m**	τ_y**/m**	τ_z**/m**	x_c**/m**
1	-15.69	0.204	0.058	127
2	6.85	0.161	0.061	124
3	-7.24	0.093	0.232	96
4	-3.99	0.085	0.201	99
5	-44.97	0.114	0.065	72
6	-42.52	0.249	0.343	74
7	-42.98	0.201	0.048	81
8	-46.26	0.141	0.119	88

Table S4. y_c, $\sigma_y(x)$ and $\sigma_z(x)$ for each UAV flight from the sample data and the average parallel distance of the sampling plane from the emission source.

G. Random walk simulation

In order to simulate a random walk to best replicate sampling, each random walk was constrained within the sampling plane defined by the maximum extent of sampling. An example of a random walk is shown in Figure S6, in which the conditions of flight 8 from the sample data were replicated, with the target flux set to 1.81 g s^{-1}.

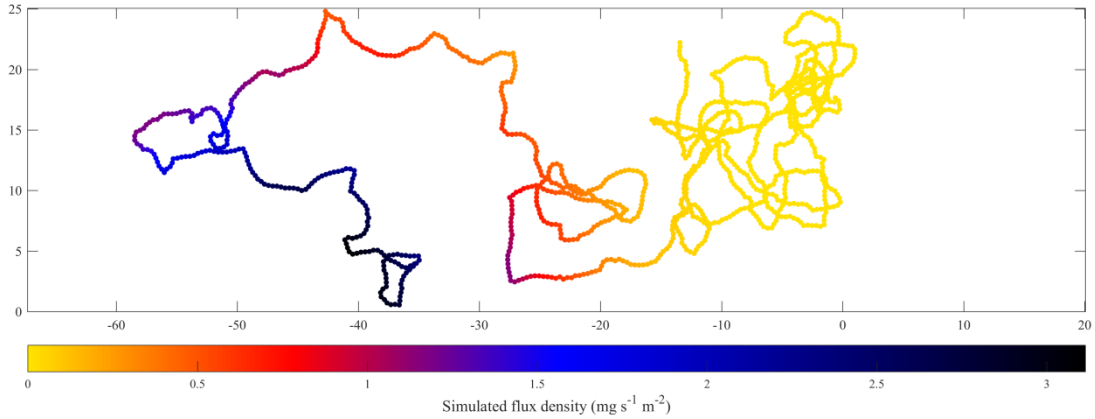

Figure S6. A virtually-generated random walk to replicate flight 8 from the sample data, with the duration of the random walk set to the equivalent time period (21 minutes). Corresponding q_{me} values are represented by the colour of each point. *z* is plotted on the vertical axis and *y* is plotted on the horizontal axis.

It was also important to test the method for simulated three-dimensional sampling, where true sampling may not be constrained to a perfect two-dimensional plane perpendicular to the wind. To test this, the *y* positions of each step were used to simulate a corresponding set of *x* positions, by assuming the sampling plane to be offset from the plane perpendicular to θ, at a constant angle. This offset angle was calculated for each flight using a linear fit to the highest and lowest 10% of real *x* and *y* position measurements.

H. Random walk simulation results

The fitting parameters for equation (14), α and β, are given in Table S5 and allow the fundamental minimum uncertainty due to random error associated with the NGI method to be calculated, by setting t to the actual duration of sampling.

UAV flight	α	β/hours
1	0.63±0.04	3.6±0.4
2	0.27±0.02	1.5±0.1
3	0.56±0.04	1.4±0.1
4	0.31±0.02	1.5±0.1
5	0.90±0.05	1.5±0.1
6	1.60±0.51	1.4±0.5
7	0.77±0.04	2.9±0.3
8	0.64±0.04	2.0±0.2

Table S5. Flux convergence parameters required to approximate the fundamental threshold uncertainty associated with flux measurements as a function of sampling time, which are unique for each flight in the sample data.

In order to analyse the convergence in A with increasing t, scale factor as a function of t ($sf(t)$) was applied to the initial uncorrected flux estimate ($F_{e,\,v,\,i}$), using equation (B), to derive corrected $F_{e,\,v}$ values as a function of t. $sf(t)$ took into account the effects of a negative flux bias due to limited temporal sampling. By removing this flux bias (see Figure S7 for example), the change in random uncertainty in $F_{e,\,v}$ with increasing t could therefore be assessed.

(B) $$F_{e,\,v} = F_{e,\,v,\,i} \cdot (1+sf(t))$$

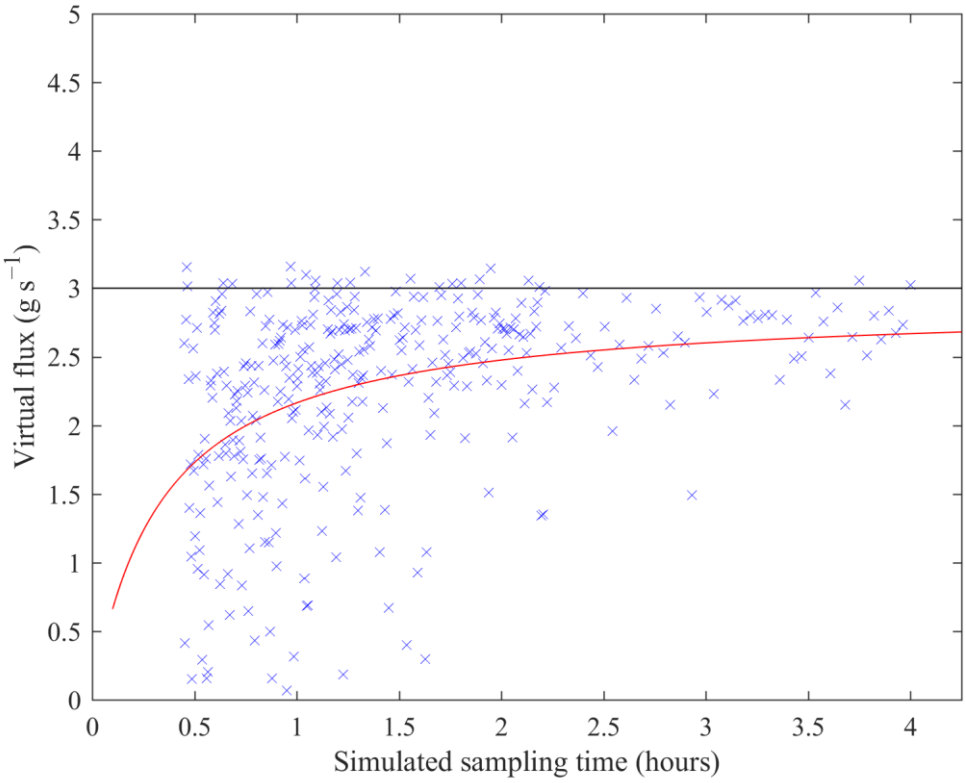

Figure S7. $F_{e,\,v,\,i}$ values, simulating flight 3 from the sample data, as a function of t (blue crosses), plotted against left-hand axis, with F_t (black line) also shown. The fit used to derive $sf(t)$ is given as a red line.

For the sample data, $sf(t)$ was calculated by quantifying the flux bias as a function of t. 180 random walk simulations were repeated at 15 different values of t up to four hours. Each test was used to derive $\overline{F_{e,\,v}}$ as a function of t. The difference between $\overline{F_{e,\,v}}$ and F_t as a function of t was used to derive discrete values of $sf(t)$ to which a decay was applied using equation (C), characterised by two coefficients (C_1 and C_2).

(C) $$sf(t) = C_1 + \frac{C_2}{t}$$

The uncertainty in A_f (ΔA_f) was calculated from the error in α ($\Delta\alpha$) and the error in β ($\Delta\beta$), where t was the duration of sampling, using equation (D). The uncertainty in $t_{1\%}$ ($\Delta t_{1\%}$) was calculated from $\Delta\alpha$ and $\Delta\beta$, using equation (E).

(D) $$\Delta A_f = A_f \cdot \left(\left(\frac{\Delta\alpha}{\alpha}\right)^2 + \left(\frac{t\cdot\Delta\beta}{\beta^2}\right)^2\right)^{\frac{1}{2}}$$

(E) $$\Delta t_{1\%} = \left(\left(\Delta\beta \cdot \ln\left(\frac{0.01}{\alpha}\right)\right)^2 + \left(\beta \cdot \frac{\Delta\alpha}{\alpha}\right)^2\right)^{\frac{1}{2}}$$

In order to test the modified mass balance method for unrestrictive sampling, the virtual flux analysis was repeated at a fixed sampling time of twelve hours (relative to the size of the original sampling plane) and repeated 60 times for each flight. The average value of $F_{e,v}$ for each test is given in Table S6.

UAV flight	F_t/g s^{-1}	**Average** $F_{e,v}$ /g s^{-1}	**Virtual flux percentage bias**
1	3	2.95±0.25	-1.52%
2	3	2.96±0.03	-1.43%
3	3	2.98±0.05	-0.57%
4	3	3.00±0.03	-0.15%
5	3	2.99±0.04	-0.40%
6	3	2.98±0.06	-0.64%
7	1.5	1.49±0.03	-0.82%
8	1.5	1.49±0.03	-0.35%

Table S6. Average virtual test F_e values for each flight in the sample data with eight hours of random sampling of a static plume.

I. Initial flux results, uncertainty factors and uncertainty analysis

All initial flux values and corresponding ΔF_-, ΔF_+ and ΔF_m values displayed in Figure 4 are given in Table S7. ΔF_-, ΔF_+ and ΔF_m values are given as fractional uncertainty contributions.

UAV flight	F_e/kg s^{-1}	$\Delta F_-/F_e$	$\Delta F_+/F_e$	$\Delta F_m/F_e$
1	0.00636	0.775	1.500	0.227
2	0.00314	0.827	1.269	0.220
3	0.00449	0.747	1.193	0.187
4	0.00425	0.710	1.083	0.161
5	0.00203	0.766	1.377	0.178
6	0.00747	0.832	1.524	0.181
7	0.00204	0.747	1.427	0.226
8	0.00182	0.672	1.207	0.138

Table S7. Initial flux values and corresponding fractional lower and upper uncertainty bounds, for each flight from the sample data.

The components of ΔF_m can further be investigated by isolating individual contributing uncertainty components in equation (3). ΔF_m due to wind speed variability ($\Delta F_{m,\,U(z)}$) was obtained using each "j" value of q_{me}, $U(z)$ and $\sigma_U(z)$ value in equation (F). ΔF_m due to uncertainty in the methane mass density ($\Delta F_{m,\,\rho}$) was obtained using each "j" value of q_{me} along with ρ and σ_ρ value in equation (G). ΔF_-^{me} due to the combined effects of instrumental uncertainty and uncertainty in the background concentration ($\Delta F_{m,\,ib}$) was obtained using each "j" value of q_{me}, $[CH_4]_{me}$ and $\sigma_i([CH_4])$ value in equation (H). These values are given in Table S8 as a fraction of ΔF_m.

(F) $$\Delta F_{m,\,U(z)} = \pm\frac{F_e \cdot \Sigma_j\left(\left|\frac{q_{mej}\cdot\sigma_U(z)_j}{U(z)_j}\right|\right)}{\Sigma_j\left(\left|q_{mej}\right|\right)}\Delta F_m = \pm F_e \cdot \left(\frac{\Sigma_j\left({q_{mej}}^2\cdot\left(\frac{\sigma_U(z)}{U(z)}\right)^2\right)}{\Sigma_j\left({q_{mej}}^2\right)}\right)^{\frac{1}{2}}$$

(G) $$\Delta F_{m,\,\rho} = \pm F_e \cdot \frac{\sigma_\rho}{\rho}$$

(H) $$\Delta F_{m,\,ib} = \pm F_e \cdot \left(\frac{\Sigma_j\left({q_{mej}}^2\cdot\left(\frac{{\sigma_{AI}}^2+\left([CH_4](y,z,x)_j^2\cdot\sigma_i([CH_4])_j\right)^2+{\sigma_b}^2}{\left([CH_4](y,z,x)_j-[CH_4]_0\right)^2}\right)\right)}{\Sigma_j\left({q_{mej}}^2\right)}\right)^{\frac{1}{2}}$$

UAV flight	ΔF_m	$\Delta F_{m,\,U(z)}/\Delta F_m$	$\Delta F_{m,\,\rho}/\Delta F_m$	$\Delta F_{m,\,ib}/\Delta F_m$
1	0.001440	0.996	0.001	0.003
2	0.000691	0.996	0.001	0.004
3	0.000841	0.999	0.002	0.001
4	0.000682	0.992	0.002	0.005
5	0.000361	0.999	0.001	0.001
6	0.001355	0.998	0.001	0.001
7	0.000461	0.998	0.003	0.001
8	0.000251	0.997	0.006	0.001

Table S8. A comparison between $\Delta F_{m,\,U(z)}$, $\Delta F_{m,\,\rho}$ and $\Delta F_{m,\,ib}$ for each flight from the sample data, as a fraction of ΔF_m.

References

Fredenslund, A. M., Rees-White, T. C., Beaven, R. P., Delre, A., Finlayson, A., Helmore, J., Allen, G., and Scheutz, C.: Validation and error assessment of the mobile tracer gas dispersion method for measurement of fugitive emissions from area sources, Waste Manage, 83, 68-78, 10.1016/j.wasman.2018.10.036, 2019.

Gardiner, T., Helmore, J., Innocenti, F., and Robinson, R.: Field Validation of Remote Sensing Methane Emission Measurements, Remote Sens-Basel, 9, article number: 956, 10.3390/rs9090956, 2017.

Turner, D. B.: Workbook of Atmospheric Dispersion Estimates: An Introduction to Dispersion Modeling, 2 ed., CRC Press, Inc., Boca Raton, United States of America, 1994.